# Growth of HfN thin films by reactive high power impulse magnetron sputtering

D. Ö. Thorsteinsson[1] and J. T. Gudmundsson[1,2,a]
[1]*Science Institute, University of Iceland, Dunhaga 3, IS-107 Reykjavik, Iceland*
[2]*Department of Space and Plasma Physics, School of Electrical Engineering and Computer Science, KTH–Royal Institute of Technology, SE-100 44 Stockholm, Sweden*

(Received 10 February 2018; accepted 21 March 2018; published online 29 March 2018)

Thin hafnium nitride films were grown on $SiO_2$ by reactive high power impulse magnetron sputtering (HiPIMS) and reactive direct current magnetron sputtering (dcMS). The conditions during growth were kept similar and the film properties were compared as growth temperature, nitrogen flow rate, and in the case of HiPIMS, duty cycle were independently varied. The films were characterized with grazing incidence X-ray diffraction (GIXRD), X-ray reflection (XRR) and X-ray stress analysis (XSA). HiPIMS growth had a lower growth rate for all grown films, but the films surfaces were smoother. The film density of HiPIMS deposited films grown at low duty cycle was comparable to dcMS grown films. Increasing the duty cycle increased the density of the HiPIMS grown films almost to the bulk density of HfN as well as increasing the growth rate, while the surface roughness did not change significantly. The HiPIMS grown films had large compressive stress while the dcMS grown films had some tensile stress. The dcMS grown films exhibit larger grains than HiPIMS grown films. The grain size of HiPIMS grown films decreases with increasing nitrogen flow rate, while the dcMS grain size increased with increasing nitrogen flow rate. This work shows that duty cycle during HiPIMS growth of HfN films has a significant effect on the film density and growth rate while other film properties seem mostly unaffected.  https://doi.org/10.1063/1.5025553

## I. INTRODUCTION

Transition metal nitride films have over the years attracted attention due to their many desired physical properties. The group-IVB transition metal nitrides which crystallize in the cubic rocksalt B1-NaCl structure ($\delta$−TMN with TM = Ti, Zr, Hf) are well known as a class of technologically important thin film materials. They generally have high hardness, good thermal stability, good mechanical strength, chemical inertness, and low electrical conductivity. One of those transition metal nitrides is hafnium nitride. It has a very high thermal stability with $T_m$ = 3380°C, a relatively low electrical resistivity of 33 $\mu\Omega$cm [Ref. 1, p. 192] and the highest negative free energy of formation of all the metal nitrides, 88.2 kcal/mol.[2] It has a bulk density of 13.845 g/cm$^3$ [Ref. 3, p. 194] and reported hardness of 16.3 GPa [Ref. 1, p. 198]. In addition to the cubic $\delta$−HfN, the hafnium nitride phase diagram has several other stable phases: Hexagonal $\alpha$−Hf(N), rhombohedral $\eta$−$Hf_3N_2$ and rhombohedral $\zeta$−$Hf_4N_3$.[4]

Hafnium nitride films have previously been grown by reactive direct current diode sputtering,[5] reactive radio frequency diode sputtering,[6,7] reactive direct current magnetron sputtering,[8–17] reactive radio frequency magnetron sputtering,[18–22] reactive high power impulse magnetron sputtering,[23] plasma-assisted atomic layer deposition,[24] electron beam physical vapor deposition,[25] activated reactive evaporation (ARE),[26] pulsed laser deposition[27,28] and ion beam assisted deposition (IBAD).[29]

[a]tumi@hi.is

 

Application of HfN thin films include diffusion barriers[7,22,30] and gate electrodes[31–33] in integrated circuits, as microelectronic emitters in field emitter arrays,[18] as absorber layer in solar cells,[17] as an intermediate layer in hydrogen permeation membranes,[34] as thermal barrier coatings[25] and as hard and protective coatings on tools.[8,35]

High power impulse magnetron sputtering (HiPIMS) is a fairly new growth method where short and powerful pulses with a low repetition frequency are applied to a conventional magnetron sputter tool. The pulses generally have a length of 10 to 400 $\mu$s, a frequency of 50 to 5000 Hz, and a duty cycle of about 0.5 % to 5 % of the full period.[36] This leads to a peak power that is a few orders of magnitude higher than applied in conventional dc magnetron sputtering (dcMS). The high peak power leads to a high electron density, which in turn causes the atoms that are sputtered off the target to become mostly ionized.[36,37]

Among the group-IVB transition metal nitrides TiN thin films are used extensively for the wear protection of machine components and tools among other applications. Thus there are numerous studies of the properties of TiN thin films. Earlier it has been demonstrated that HiPIMS-deposited TiN films produce denser films at lower deposition temperatures, that have significantly lower surface roughness.[38–40] Furthermore, it has been demonstrated that HiPIMS grown TiN films have significantly lower electrical resistivity than dcMS grown films on $SiO_2$ at all growth temperatures.[41] HiPIMS grown ZrN films have also been shown to exhibit dense microstructure and smooth morphology.[42] Berg et al.[43] demonstrated that HfN thin films exhibit properties very similar to TiN thin films when grown under identical process conditions due to very similar crystal structure of the materials. They point out that higher hardness is the only fundamental property which is better for HfN than for TiN, while TiN films exhibit better wear reduction and adhesion. Abadias and Guerin[44] monitored the stress evolution during reactive dc magnetron sputtering of TiN, ZrN and TiZrN thin films. For TiN and TiZrN films they see a change from compressive stress to tensile stress as the film thickness increases. This has been suggested to be due to a stress gradient in the film.[45] The stress is highly compressive at the interface and less compressive up the film. Abadias and Guerin[44] suggested that the origin of the stress gradient arises from two competing stress generation mechanisms: growth-induced point defects due to atomic peening which leads to compressive stress, and void formation which leads to tensile stress. Furthermore, it has been demonstrated that HiPIMS grown TiN films exhibit compressive intrinsic stress and a stress gradient is absent in these films.[46]

Here we report on the growth and characterization of thin hafnium nitride films deposited by reactive HiPIMS on silicon, with 1 $\mu$m of thermally oxidized silicon oxide layer, performed in a custom built sputter chamber. The film properties are compared to films grown with dcMS sputtering in the same chamber, at similar conditions. We discuss the experimental setup and methods in Section II, the influence of the various growth conditions such as nitrogen flow rate, duty cycle, and growth temperature on the film density, surface roughness, and intrinsic stress in Section III and then give concluding remarks in Section IV.

## II. EXPERIMENTAL APPARATUS AND METHOD

The magnetron sputtering was performed in a specialized system that is described in more detail by Arnalds et al.[47] The system is made up of two chambers made of stainless steel: a small load-lock chamber, and a cylindrical sputtering chamber which is 29 cm in diameter and 25 cm in length. The substrate is loaded using the load-lock onto a stage in the main chamber, which can be raised or lowered for convenience during loading and unloading. The substrate holder is electrically isolated from the rest of the chamber, and bias can be applied to the stage (or the substrate) if desired. A heating plate is located 2 mm below the substrate. A thermocouple placed between the substrate and the heater measures the temperature during growth. The system can safely operate at substrate temperatures of up to 800°C.

Film deposition was carried out using both HiPIMS and dcMS. For the HiPIMS process the power was supplied by a SPIK1000A pulse unit (Melec GmbH) operating in the unipolar negative mode at constant voltage, which in turn was charged by a dc power supply (ADL GS30). The discharge current and voltage was monitored using a combined current transformer and a voltage divider unit (Melec GmbH) and the data was recorded with a digital storage oscilloscope (Agilent 54624A).

The hafnium target used in this work was 75 mm (3 inches) in diameter. The strength of the magnet was measured as 0.53 T in a bench setup outside of the chamber at a distance that corresponds to the surface of the target. The Ar and $N_2$ gases used are 99.999 % pure. The Ar flow rate was kept constant at 40 sccm during all sputtering processes. The growth parameters that are shared between dcMS and HiPIMS were also kept at the same values when possible. The operating pressure during growth was kept constant with a gate valve at 1.24 Pa for HiPIMS and 0.74 Pa for dcMS sputtering. The values were chosen for the most stable operation during the sputtering of the films. For most of the films the average power was kept within the range 150 – 160 W, except when duty cycle for HiPIMS was changed, which inevitably changed the average power. Attempts were made to keep the thickness of each film at 60 nm, but because of the variations in the growth rate, the thickness varied from 40 nm to 80 nm.

The substrates used for the growth of all the samples were from the same wafer of [100] monocrystalline Si from Crystec with 1 $\mu$m of thermally oxidized $SiO_2$ on top. The oxide layer has a measured density of 2.19 g/cm$^3$ and surface roughness of 0.35 nm. The substrates were cut into 9 mm × 9 mm squares to fit into the sample holder. Before growth, all the substrates were cleaned in an ultrasonic bath with acetone, methanol and isopropanol for 5 minutes each. The substrates were then rinsed with de-ionized water and blow dried with pure argon. A substrate was then placed in the vacuum chamber where it was baked for 10 minutes at 650°C before sputtering began.

Grazing incidence X-ray diffractometry (GIXRD), X-ray reflectometry (XRR) and X-ray stress analysis (XSA) were performed on a PANalytical X'pert diffractometer. The diffractometer has a hybrid monochromator/mirror on the incident side and a 0.27° collimator on the diffracted side. The collimator was removed during GIXRD and X-ray stress analysis to get a better signal to noise ratio during the measurements. The Cu-$K_\alpha$ line with wavelength 0.15406 nm was used for all measurements. A line focus was used so the beam width was approximately 1 mm.

The GIXRD measurements were performed at an incident angle of $\theta_i = 0.8°$, measuring $2\theta$ from 30° to 75° for phase identification and for grain size estimates. The angular resolution of the GIXRD measurements was 0.03°. The XRR measurements measured $2\theta$ from 0.2° to 6.2° with an angular resolution of 0.004°. Using X'pert reflectivity, the density, roughness and thickness of the films were then calculated. For X-ray stress analysis, the [111] reflection of the cubic $\delta$−HfN phase was measured for all films, since it had the highest intensity of all measured peaks. The angular resolution was 0.02° with a 16 s wait time and the films were measured with $\sin^2\psi$ from 0 to 0.75 with an increment of 0.05, yielding 16 measurements for stress evaluation for each film.

It is possible to measure residual stress in thin films with an X-ray diffractometer. If the stress is assumed to be biaxial, XRD-$\sin^2\psi$ measurement can be made, where $\psi$ represents a tilt angle of the sample with respect to the scattering plane. For the measurement, the position of a peak with specific Miller indices is measured at different tilt angles to get the change in $d$-spacing as a function of the tilt angle. The fundamental equation for an XRD-$\sin^2\psi$ stress measurement can be written as[48,49]

$$\frac{d_\psi - d_0}{d_0} = \frac{1+\nu}{E} \cdot \sigma_\psi \cdot \sin^2\psi - \frac{2\nu}{E} \cdot \sigma_\psi \tag{1}$$

where $d_\psi$ is the measured $d$-spacing as a function of $\psi$, $d_0$ is the $d$-spacing of the peak when no stress is present, $\sigma_\psi$ is the stress as a function of $\psi$ and $\nu$ and $E$ are Poisson ratio and Young's modulus respectively, both dependent on the material being measured. The measurement is performed by measuring a specific Bragg plane at a constant tilt angle $\psi$. Generally, $d_0$, $\nu$ and $E$ are all known constants of the material, so the equation can be easily rewritten as a linear equation with $\sigma_\psi$ as the slope,

$$d_\psi = \left(\frac{1+\nu}{E} \cdot d_0 \cdot \sin^2\psi - \frac{2\nu}{E} \cdot d_0\right) \cdot \sigma_\psi + d_0 \tag{2}$$

and $d_\psi$ is measured as a function of $\psi$ and plotted against the terms inside the brackets in the equation above, giving the intrinsic stress $\sigma_\psi$ as the slope of that graph. The Young's modulus (elastic modulus) for HfN films was measured as $E_{HfN}$ = 380 GPa by Török et al.[50] a value slightly lower than for the other nitrides ZrN and TiN in that study. It is argued by Nagao et al.[51] based on density-functional theory calculation that due to the strong anisotropy, the Young's modulus of HfN varies from 300 GPa to approximately 600 GPa depending on the crystallographic direction and thus difficult

to determine a single averaged value of the Young's modulus for a polycrystalline film. However, more recently, Seo et al.[11] give a measured value of 450 ± 9 GPa for HfN, a value that is essentially identical to the values observed for TiN and TaN. For the stress calculation we use this value 450 ± 9 GPa and Poisson ratio of $\nu_{HfN}$ = 0.35 from Perry.[52] It is known that the elastic modulus depends on the film density and composition, and it is expected to decrease with decreasing film density. Our films are dense so the higher value is assumed to better represent our films. When showing graphically the overall stress we show errorbars covering the elastic modulus in the range from 370 to 460 GPa.

## III. RESULTS AND DISCUSSION

HfN films were grown by HiPIMS and dcMS. In Section III A we discuss the film density, growth rate and surface roughness while independently varying the growth temperature and nitrogen flow rate. In Section III B we show the results from overall stress evaluation of the films and in Section III C we explore the influence of the duty cycle on the film density, growth rate, stress and surface roughness.

### A. Influence of growth temperature and nitrogen flow rate

Figure 1 shows the GIXRD scans of both HiPIMS and dcMS grown films at various nitrogen flow rates. The GIXRD scans are used to determine the crystal structure and composition of the films as well as to calculate the grain size of the [111] and [200] crystallites. All of the films were characterized as cubic $\delta$−HfN, with the [111], [200], [220] and [311] peaks visible in all of the films while the [222] peak is visible in some of the films. The position of the peaks of the HiPIMS grown films is considerably shifted to lower $2\theta$ values in all of the films. However, very little shift is seen in the peaks from the dcMS grown films, and they follow the expected peak positions for the cubic $\delta$−HfN rocksalt structure given in the ICDD Reference Pattern 03-065-4298. The peak width also changes drastically with increasing nitrogen flow rate for the HiPIMS grown films, but seems to decrease in dcMS grown films. In Figure 2 the GIXRD scans are shown as a function of the growth temperature. Unlike for the films shown in Figure 1, not all of the films exhibit the cubic $\delta$−HfN phase. The dcMS grown film at 600°C fits the hexagonal $HfN_{0.4}$ phase as given in the ICDD Reference Pattern 00-040-1277 most closely, with a strong [103] peak. Other peaks fitting the hexagonal $HfN_{0.4}$ were also observed, but with much lower intensities than the [103] peak. Again, there is a shift in the peaks of the HiPIMS grown $\delta$−HfN films to lower $2\theta$ values which is not seen in the dcMS grown films.

Figure 3 shows the density, growth rate and surface roughness of the films, calculated from the XRR measurements, as a function of nitrogen flow rate. The density of HiPIMS grown films, shown in Figure 3(a), starts off higher than for the dcMS grown films, with a maximum of 13.3 g/cm$^3$, while the dcMS grown films exhibit a maximum density of 13.14 g/cm$^3$. For comparison the theoretical bulk density of HfN is 13.84 g/cm$^3$ [Ref. 3, p. 194]. However, the density quickly drops

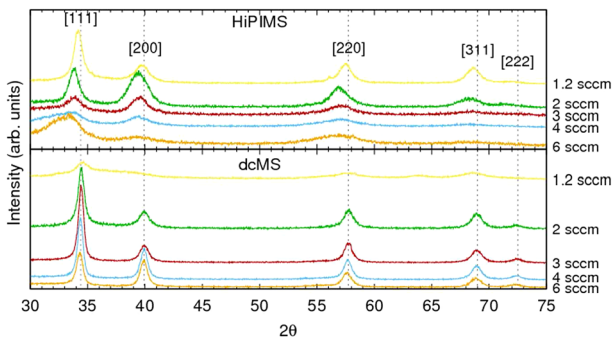


FIG. 1. The GIXRD scans of dcMS and HiPIMS grown films at various nitrogen flow rates. The films were grown at 400°C with Ar flow of 40 sccm while the nitrogen flow rate is varied. The scans have been shifted up for better graphical representation.

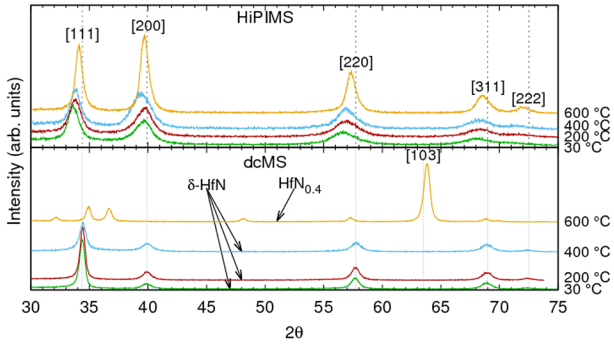


FIG. 2. The GIXRD scans of dcMS and HiPIMS grown films for various growth temperatures. The films were grown at a nitrogen flow rate of 2 sccm and Ar flow of 40 sccm. The scans have been shifted up for better graphical representation.

with increasing nitrogen flow rate, reaching a minimum for HiPIMS grown films of 10.81 g/cm$^3$ at 6 sccm nitrogen, while dcMS grown films stabilize at 12.1 g/cm$^3$ for nitrogen flow rates between 3 to 6 sccm. Johansson et al.[53] explored the variation in the density of grown films with nitrogen flow rate for reactively dcMS sputtered HfN films. They found that with increasing nitrogen flow rate, the density drops from a maximum of about 13.5 g/cm$^3$ to 11 g/cm$^3$. Their nitrogen partial pressure was higher than used for the films grown in this work. The variation in density is more pronounced in Johansson's work, with the films going both closer to the bulk density and getting less dense than

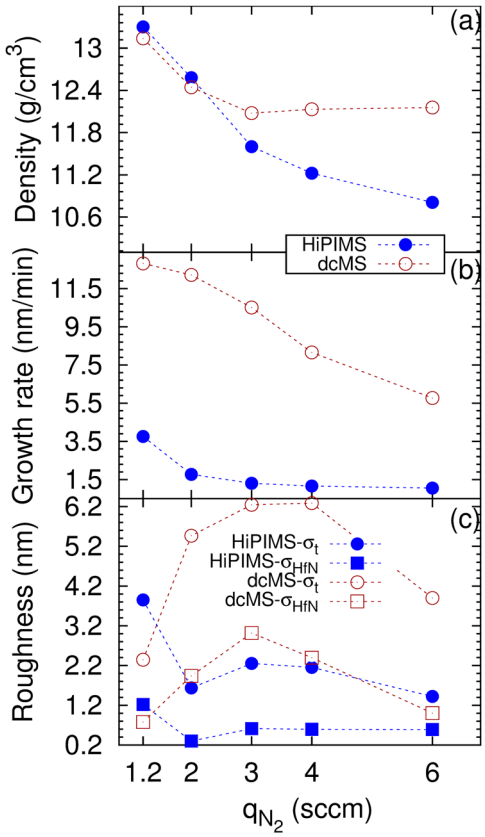


FIG. 3. (a) The film density, (b) growth rate, and (c) the surface roughness for dcMS and HiPIMS grown films as a function of nitrogen flow rate. The films were grown at 400°C with Ar flow of 40 sccm. $\sigma_{\mathrm{HfN}}$ is the roughness of the HfN layer of the films and $\sigma_{\mathrm{t}}$ is the total roughness of all layers needed to fit the films.

those seen in this work. Smith[5] reports density values for HfN films grown with dc diode sputtering to be 11.9 g/cm$^3$, lower than that of the dcMS grown films here, but higher than observed for HiPIMS grown films at 3 sccm $N_2$ or higher.

The film growth rate is shown in Figure 3(b) as a function of nitrogen flow rate. We note that the deposition rate decreases with increasing nitrogen flow rate. For nitrogen flow rate of 1.2 sccm the ratio of the deposition rates is $DR_{HiPIMS}/DR_{dcMS} = 0.3$ and drops to $DR_{HiPIMS}/DR_{dcMS} = 0.12$ for nitrogen flow rate of 6 sccm. The film surface roughness is shown in Figure 3(c) as a function of the nitrogen flow rate. In order to properly fit the XRR scans we had to include a low density surface layer. Thus we present the roughness as the roughness of the HfN layer $\sigma_{HfN}$ and the total roughness $\sigma_t$ which is the sum of $\sigma_{HfN}$ and the thickness of the surface layer. The total roughness $\sigma_t$ and the roughness of the HfN layer $\sigma_{HfN}$ is lower for the HiPIMS grown films, excluding the film grown at 1.2 sccm $N_2$. For HiPIMS grown films, the roughness of the HfN layer was between 0.3 nm and 1.2 nm, with the second highest value of only 0.6 nm, while the roughness of the same layer in dcMS grown films was between 0.8 nm and 3 nm.

Figure 4 shows the density, growth rate and surface roughness of the films as a function of growth temperature. The film density is higher and surface roughness is lower for all growth temperatures for HiPIMS grown films, and the growth rate is always lower. The film density increases with increased growth temperature, increasing from 11.9 g/cm$^3$ to 13.1 g/cm$^3$ for HiPIMS growth as the growth temperature is increased from room temperature to 600°C as shown in Figure 4(a). For dcMS grown films the density increases from 10.7 g/cm$^3$ to 12.4 g/cm$^3$ for the same growth temperature range. The growth rate for HiPIMS is 13.7 % to 17 % of the dcMS growth rate as seen in Figure 4(b). The roughness of the HfN layer for HiPIMS grown films ranges from 0.2 nm to 0.83 nm when grown at

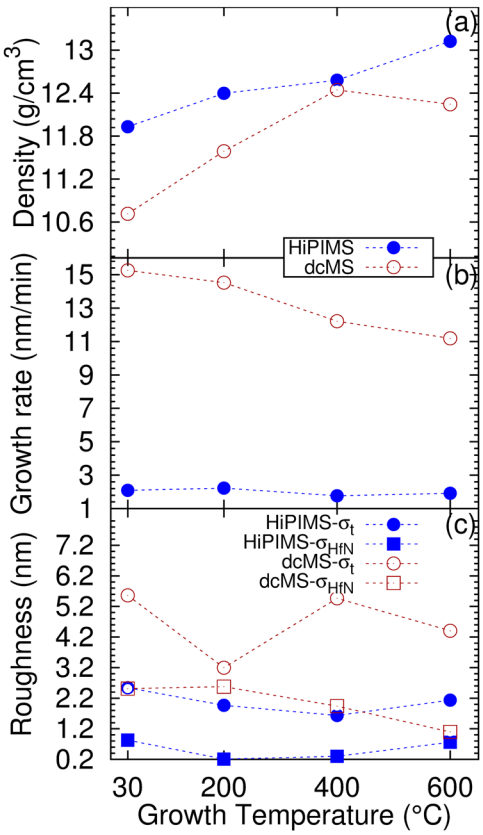


FIG. 4. (a) The film density, (b) growth rate, and (c) the surface roughness for dcMS and HiPIMS grown films as a function of growth temperature. The films were grown at nitrogen flow rate of 2 sccm and Ar flow rate of 40 sccm. $\sigma_{HfN}$ is the roughness of the HfN layer of the films and $\sigma_t$ is the total roughness of all layers needed to fit the films.

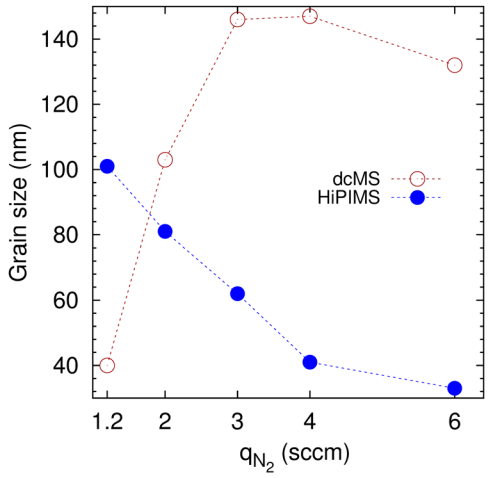


FIG. 5. The grain size of the $\delta$−HfN [111] crystallites as a function of $N_2$ flow rate for films grown by dcMS and HiPIMS at 400°C and Ar flow rate of 40 sccm.

room temperature and films grown at 600°C are significantly rougher than the films grown at 200°C and 400°C as seen in Figure 4(c). Meanwhile, the same layer in dcMS grown films has a roughness of 2.6 nm to 1.1 nm, decreasing with increased growth temperature.

The grain size was calculated from the GIXRD scans shown in Figures 1 and 2 using the Scherrer formula. Figure 5 shows the size of the [111] crystallites of the $\delta$−HfN films as a function of nitrogen flow rate. The peak broadening observed in Figure 1 indicates that the grain size in the HiPIMS grown films drops with increasing nitrogen flow rate, from an estimated value of 100 nm down to 33 nm. Meanwhile, the grain size of dcMS grown films starts at a minimum of 47 nm for nitrogen flow rate of 1.2 sccm but increases with increasing flow rate up to a maximum of 147 nm. The [200] grains exhibit the same trend, the grain size drops with increasing nitrogen flow rate for HiPIMS grown films but for dcMS grown films it increases with increasing nitrogen flow rate (not shown). Also the [200] crystallites are in general slightly smaller than the [111] crystallites. Figure 6 shows the grain size of the [111] crystallites of the cubic $\delta$−HfN films for both dcMS and HiPIMS grown films as a function of temperature. The grain size of dcMS grown films is larger for all growth temperatures, with the grain size reaching a maximum of 175 nm for growth temperature of 200°C

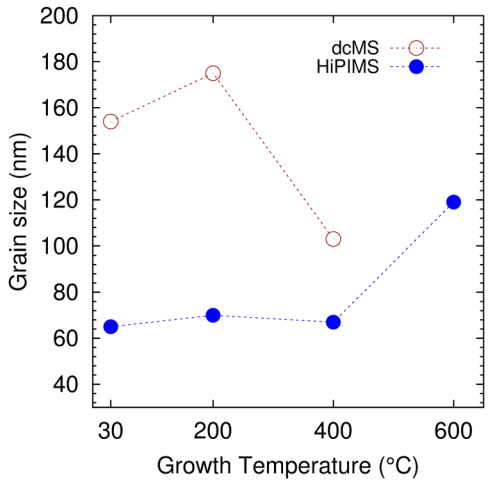


FIG. 6. The grain size of the $\delta$−HfN [111] crystallites as a function of growth temperature for films grown by dcMS and HiPIMS at $N_2$ flow rate of 2 sccm and Ar flow rate of 40 sccm.

to a minimum of 103 nm for growth temperature of 400°C. For HiPIMS grown films the grain size stayed almost constant from room temperature to 400°C, with the grain size being 65 nm to 70 nm, but for growth temperature of 600°C the grain size almost doubles, increasing to 119 nm. The growth temperature dependence of the [200] crystallite size shows approximately the same trend as is seen for the [111] crystallites (not shown). It is difficult to compare grain sizes since the values obtained often depend on the measurement settings, the devices used and the grain size is often dependent on the thickness of the films. However, trends in grain size can be compared to some extent. García-González et al.,[10] while depositing HfN films by reactive dcMS, note that grain size did not change significantly with increasing nitrogen flow rate. They report grain size in the range 7.9 – 9.1 nm, increasing with decreasing nitrogen flow rate. However, they do not explicitly state which peaks are used for the calculation of the grain size in their work. This does not agree with the findings in this work, as the grain size of both the [111] and [200] crystallites are much larger and their size varies with nitrogen flow rate.

### B. Stress in HfN films

The big shift in the peak locations of the GIXRD measurements in the HiPIMS grown films has several possible explanations. The most likely one for such a significant shift was deemed to be intrinsic stress in the films, since energetic ions are known to exist in HiPIMS deposition[54] and those can cause atomic peening in the film. Stress in thin films can have a significant influence on the performance and reliability of passive and active thin film components in modern devices. Shift in the position of the [111] peak was therefore measured and the stress evaluated for all films over different tilt angles. The overall stress in the film measured *ex-situ* at room temperature comprises the intrinsic stress and thermal stress $\sigma_{th}$ that develops upon cooling down to room temperature after growth. The thermal stress contribution can be estimated from the difference in the linear thermal expansion coefficient between the HfN film ($\alpha_{HfN} = 6.9 \times 10^{-6}$ K$^{-1}$ [Ref. 3, p. 194]) and the $SiO_2$ substrate ($\alpha_{SiO_2} = 5\times10^{-7}$ K$^{-1}$ for thermally oxidized $SiO_2$[55]) using $\sigma_{th} = E_{HfN}/(1-\nu_{HfN})\times(\alpha_{HfN}-\alpha_{SiO_2})\times\Delta T$, where $E_{HfN}$ and $\nu_{HfN}$ are the Young modulus and Poisson ratio of the HfN film, respectively, and $\Delta T$ is the temperature difference between deposition temperature and room temperature. The contribution of the thermal stress is +0.75 GPa for growth at 200°C, +1.64 GPa for growth at 400°C, and +2.53 GPa for growth at 600°C. Thus the contribution of thermal stress to the overall stress is quite significant in particular for the higher growth temperatures.

The overall stress observed in the films grown at various growth temperatures is shown in Figure 7. The calculations are made assuming $E_{HfN} = 450$ GPa and the errorbars show the variation in the intrinsic stress if the elastic modulus is in the range $370 \le E_{HfN} \le 460$.

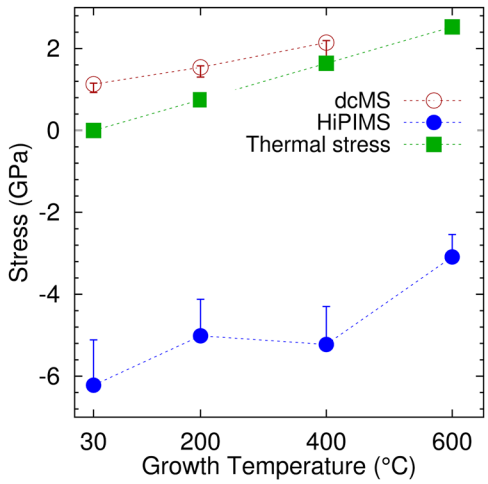


FIG. 7. The overall stress and the thermal stress in HfN films as a function the growth temperature while the argon flow rate was 40 sccm and the nitrogen flow rate was 2 sccm. The stress was measured with the $\sin^2\psi$ method over the [111] peak.

Negative stress values indicate compressive stress while positive values indicate tensile stress. The dcMS grown films exhibit some tensile stress that increases with increasing growth temperature, from 1.1 GPa at room temperature to 2.1 GPa at 400°C. In Figure 7 we also show the thermal stress expected in the films grown at the various temperatures after cooling down to room temperature. We note that much of the stress observed in the dcMS grown films is due to thermal stress. Meanwhile, HiPIMS grown films exhibit high compressive stress. This compressive stress reduces with increasing growth temperature, from 6.2 GPa at room temperature growth to 2.9 GPa at 600°C. The decrease in the overall stress with increase in growth temperature is probably mainly due to contribution from thermal stress.

Figure 8 shows the overall stress observed in both HiPIMS and dcMS grown films as a function of nitrogen flow rate while the argon flow rate was kept constant at 40 sccm and the substrate temperature is kept at 400 °C. The film grown at the lowest nitrogen flow rate 1.2 sccm shows compressive stress of 1.2 GPa. The dcMS grown films quickly gain tensile stress with increasing nitrogen flow rate, with a maximum of 2.1 GPa for nitrogen flow rate of 2 sccm, but then it drops down slowly to just below 0 GPa at 6 sccm of nitrogen, indicating slightly compressive stress. The tensile stress indicates that voids exist in the films. However, the HiPIMS grown films exhibit a large compressive stress for all nitrogen flow rates, increasing from 2.1 GPa to 5.1 GPa. The compressive stress is likely caused by growth-induced point defects which appear due to atomic peening as a result of highly ionized flux towards the substrate. The maximum compressive stress for HiPIMS grown films is at 2 sccm of nitrogen, the same value that gave the maximum tensile stress for dcMS grown films. The difference in overall stress between HiPIMS and dcMS grown films at 2 sccm is 7.3 GPa, showing that there is a big difference between the two growth methods.

Nowak and Maruno[20] found that the stress of their HfN films grown by reactive radio frequency diode sputtering on Si substrate was always compressive, and the stress decreased with increasing total pressure. They also applied bias to the Si substrate, which drastically increased the intrinsic stress of the films up to a maximum of about 5.5 GPa. Machunze and Janssen[56] demonstrate compressive stress in TiN films grown with reactive dcMS, both unbiased and with a bias of -125 V. The compressive stress increases when bias is applied. The increase in compressive stress with increased bias can be compared to the higher compressive stress observed for HiPIMS grown films compared to dcMS grown films. The bias increases energy of ions bombarding the substrate, similar to the increased ion energy during HiPIMS deposition, which causes atomic peening in the film. Furthermore TiN films grown by HiPIMS have been shown to exhibit compressive intrinsic stress that increases when bias of -125 V is applied to the substrate during growth.[46]

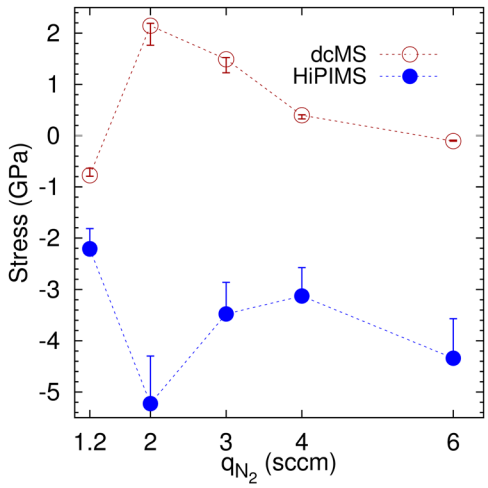


FIG. 8. The overall stress in HfN films as a function of nitrogen flow rate while the argon flow rate was 40 sccm and the substrate temperature is kept at 400°C. The stress was measured with the $\sin^2\psi$ method over the [111] peak.

### C. The effect of duty cycle

The different operation modes in HiPIMS have a significant effect on the shape of the HiPIMS pulse, because of the changes in the target surface condition and thus secondary electron emission, sputter yield and therefore the discharge current. To be able to identify whether the HiPIMS growth process is operated in poisoned or metal mode, the change of the discharge current waveform when the target transitions from metal to poisoned mode has to be explored. One of the parameters affecting poisoning is the duty cycle.

Figure 9 shows the effect of changing the pulse repetition frequency during reactive HiPIMS sputtering of a hafnium target in an $Ar/N_2$ mixture. Applied voltage, nitrogen flow rate and total pressure were kept constant at 550 V, 2 sccm and 1.24 Pa, respectively. We note that the discharge current increases rapidly with decreasing repetition frequency. Lower repetition frequency translates to longer time between pulses which gives HfN more time to form on the target surface, thus increasing the poisoning of the target. Operating at frequencies under 12 Hz resulted current values above the maximum allowed value of the power source, which then cut off the pulse and made the process very unstable. Both the shape of the pulses and the maximum current levels can later be compared to pulses recorded during growth in order to estimate the poisoning of the target during sputtering.

The discharge current waveforms of HiPIMS pulses have been investigated in an attempt to understand the HiPIMS process better and to stabilize the sputtering process. Magnus et al. explored the discharge current waveforms for reactive HiPIMS sputtering with a titanium target in $Ar/O_2$[57] and $Ar/N_2$[58] mixtures. For pure (non-reactive) titanium sputtering, the current discharge waveforms do not change as the repetition frequency is varied, and the current remains the same. For titanium target in $Ar/N_2$ mixture the current increases when the pulse frequency is lowered while the shape of the waveform is maintained. This is not the case for reactive sputtering of titanium in $Ar/O_2$ mixture. When the target is poisoned the discharge current increases almost linearly with time up to a very high levels until the pulse is cut off, so the current waveform appears triangular.[57] Similar current increases have been seen for various combinations of reactive gas and target materials.[59] In order to understand the cause of this discharge current increase an ionization region model of reactive sputtering of a Ti target in $Ar/O_2$ mixture was developed.[60] It was found that during metal mode, $Ti^+$ and $Ar^+$ ions have an equal contribution to the current, but in poisoned mode the current is dominated by $Ar^+$ -ions, caused by recycling of the working gas. It was also concluded that the triangular shape of the discharge current is caused by the recycling of the working gas. Furthermore, it has been demonstrated recently that to maintain these high discharge currents a recycling of either the process gas or the sputtered material is needed.[61] However, the current waveform observed here for Hf target in $Ar/N_2$ mixture does not become triangular nor does it maintain the shape observed at high repetition frequency as the frequency is lowered. Therefore, reactive sputtering of hafnium

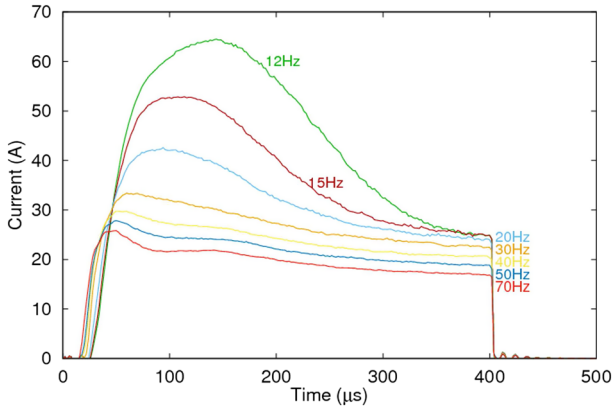


FIG. 9. The discharge current waveforms during reactive HiPIMS of hafnium in an $Ar/N_2$ 40 sccm/2 sccm mixture while changing pulse frequency. The discharge pressure was 1.24 Pa and the applied voltage was 550 V.

in $Ar/N_2$ mixture likely follows a combination of processes as it increases more significantly earlier in the pulse. The current waveform seen in Figure 9 could be dictated by self-sputter recycling or a combination of self-sputter recycling and process gas recycling. Earlier we have shown that the dominating mechanism for gas rarefaction in HiPIMS discharges is ionization losses and only about 30 % is due to the sputter wind kick-out process.[62] Furthermore, the time durations of the high-current transient, and of the rarefaction maximum, are determined by the time it takes to establish a steady-state diffusional refill of process gas from the surrounding volume. As the repetition frequency is lowered more time is allowed for the refill to take place and thus there are more atoms to become ionized and the current peak at the start of the next pulse is higher.

To see the effect of poisoning on the film properties, we compare films grown under different duty cycles. The films discussed in Section III A were grown at a repetition frequency of 75 Hz, pulse length of 150 $\mu$s and a duty cycle of 1.125 %. A few additional samples were grown at nitrogen flow rate of 2 sccm, growth temperature of 400°C with a repetition frequency of 12 Hz and 70 Hz and a pulse length of 400 $\mu$s, which gives a duty cycle of 0.48 % and 2.8 %, respectively. To see the effect of a higher duty cycle, a growth temperature series was also grown at 2 sccm $N_2$ with a duty cycle of 2.8 %. Lastly, two more films were grown at 4 sccm $N_2$ at a growth temperature of 400°C, pulse length of 400 $\mu$s and a frequency of 70 Hz and 140 Hz, which gives a duty cycle of 2.8 % and 5.6 %, respectively. As was discussed above lower duty cycle means that the target is more poisoned. Since a duty cycle of 0.48 % was the lowest duty cycle that was still stable, the target was then the most poisoned. Also higher duty cycle means that the target is closer to metal mode. The films grown with higher duty cycle exhibit a much higher density than both the dcMS grown films and the HiPIMS grown films with a lower duty cycle. The film density also remained almost constant as a function of growth temperature, with the room temperature grown film having the lowest density of 13.2 g/cm$^3$ and the highest being for growth temperature of 200°C with a density of 13.3 g/cm$^3$. As was mentioned above, the maximum density for HiPIMS grown films with duty cycle of 1.125 % was 13.1 g/cm$^3$ at 600°C and 12.4 g/cm$^3$ for dcMS growth at 400°C. Growth rate per joule is also greatly increased when duty cycle is increased. For duty cycle of 1.125 % the growth rate of HiPIMS was 13.7 % to 17 % of the dcMS growth rate, but after increasing duty cycle to 5.6 %, it is in the range 23.7 % to 29.6 % of the dcMS growth rate, almost doubling the normalized growth rate by increasing the duty cycle. Increasing the duty cycle has very little effect on the surface roughness, with the HfN layer having a roughness in the range from 0.5 nm to 0.75 nm for higher duty cycle while the same layer for lower duty cycle is 0.2 nm to 0.83 nm. Like before, the HiPIMS grown films have a much lower roughness, at all growth temperatures, than dcMS grown films. Figure 10 shows the effect of changing duty cycle on the film density, thickness per kJ and surface roughness while keeping growth temperature and nitrogen flow rate constant, at 400°C and 2 sccm, respectively. Films grown at nitrogen flow rates of 2 sccm and 4 sccm are compared. The film density (Figure 10(a)) and normalized growth rate (Figure 10(b)) are greatly improved by increasing the duty cycle, with the density approaching the bulk density of HfN of 13.8 g/cm$^3$. The growth rate seems to increase linearly with increased duty cycle as shown in Figure 10(b), and by increasing the duty cycle by a factor of six for films grown at 2 sccm $N_2$, the normalized growth rate increased by 250 %. Meanwhile, the growth rate at 4 sccm $N_2$ tripled when the duty cycle was increased by a factor of 5. The roughness does not change significantly with increasing duty cycle, with the changes being within 0.3 nm for the HfN layer at both flow rates as seen in Figure 10(c).

Figure 11 shows the overall stress measured in the HiPIMS grown films at 400°C as a function of the duty cycle. The measured stress in all of the films is compressive, and it increases significantly with increasing duty cycle for both nitrogen flow rates measured. At 2 sccm $N_2$, the overall stress increases from 3.9 GPa to 6.2 GPa, while for 4 sccm $N_2$ it increases from 3.1 GPa to 5.9 GPa. The stress matches the greatest stress measured in the films before, which was 6.2 GPa at room temperature growth and at an $N_2$ flow rate of 2 sccm. For the stress calculation the elastic modulus is assumed to be 450 GPa, and the errorbars show the range in the stress when the elastic modulus is allowed to vary in the range 370 – 460 GPa. Comparing the films grown with higher duty cycle to other works, the film density is greater, for all nitrogen flow rates, than that reported by Smith[5] for films grown by reactive rf diode sputtering. For high duty cycles the density for high flow rates is also higher than that reported by Johansson et al.[53] grown by reactive dc magnetron sputtering.

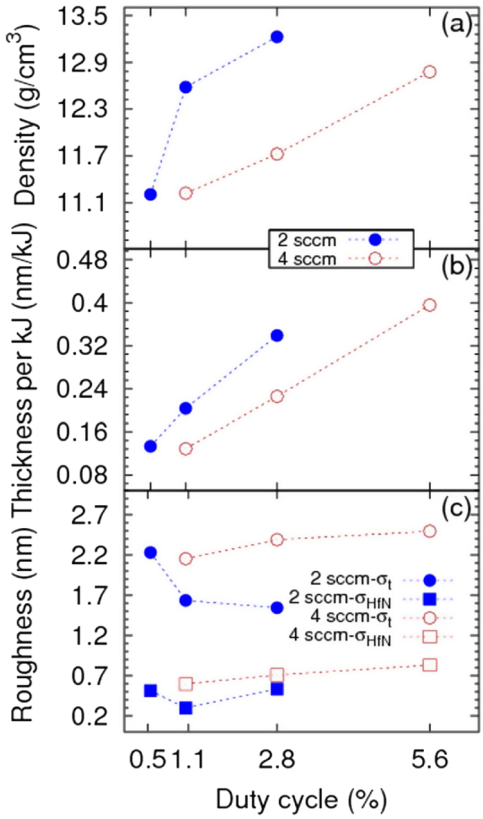


FIG. 10. The (a) film density, (b) normalized growth rate, and (c) roughness for different nitrogen flow rates as a function of duty cycle for HiPIMS grown films. $\sigma_{HfN}$ is the roughness of the HfN layer of the films and $\sigma_t$ is the total roughness of all layers needed to fit the films. The pressure was 1.24 Pa.

The growth rate also increases significantly, almost doubling for every kJ put in when the duty cycle was increased. The surface roughness of the HiPIMS grown films with higher duty cycle is still lower than the roughness of the films grown by García-González et al.[10] by reactive dcMS and lower than the roughness reported by Yu et al.[33] by reactive dc sputtering.

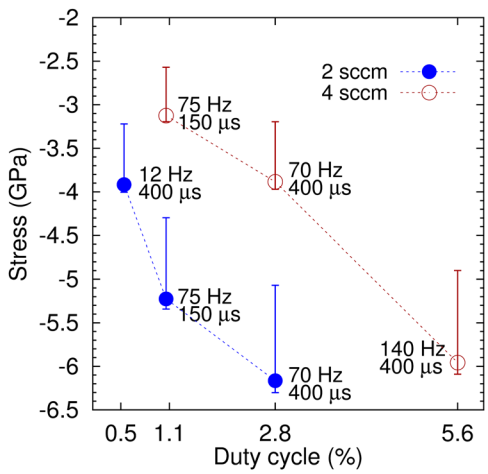


FIG. 11. The film overall stress as a function of duty cycle for HiPIMS grown films at 400°C for two different nitrogen flow rates. The pressure was 1.24 Pa.

The overall stress in the HiPIMS grown films is seen to become even more compressive as the duty cycle is increased. The increasing compressive stress can not be caused by a lack of atom mobility that can be seen for the room temperature grown film shown in Figure 7. It is more likely that the cause is the increased ion bombardment because of the more frequent and longer pulses of the films grown with higher duty cycle. This is similar to the effect seen by Nowak and Maruno[20] and by Machunze and Janssen[56] where increased substrate bias greatly increased the compressive stress in the film. Furthermore, it has been observed that HiPIMS deposition of TiN thin films results in compressive stress.[46]

## IV. CONCLUSION

Here the growth of hafnium nitride thin films using both dcMS and HiPIMS has been demonstrated. First the growth temperature was varied while keeping other variables constant, then nitrogen flow rate was varied while other variables were kept constant. Lastly, the duty cycle during the HiPIMS growth was increased, and growth temperature and nitrogen flow rate were again varied while other variables were kept constant. The HiPIMS grown films generally have a smoother surface than dcMS grown films, and the growth rate is always much lower for HiPIMS deposition than it is for dcMS. The density of HiPIMS grown films at low duty cycle is similar to dcMS grown films at low nitrogen flow rates, but decreases as the flow rate increases. However, when the duty cycle is increased, the density approaches the bulk density of HfN films for low nitrogen flow rate and is considerably higher than for both dcMS and HiPIMS grown films at higher flow rates. The growth rate also almost doubles when high duty cycle is compared to low duty cycle as a function of average power. This is thought to be related to the target being less poisoned during sputtering at higher duty cycles, which is shown to have an effect on both sputtered films and sputtering rate. The dcMS grown films exhibit tensile overall stress while the HiPIMS grown films exhibit compressive stress.

## ACKNOWLEDGMENTS

This work was partially supported by the Icelandic Research Fund Grant No. 163086 and the Swedish Government Agency for Innovation Systems (VINNOVA) contract no. 2014-04876.

[1] H. O. Pierson, *Handbook of Refractory Carbides and Nitrides* (Noyes Publications, Westwood, New Jersey, 1996).
[2] M. Wittmer, Journal of Vacuum Science and Technology A **3**, 1797 (1985).
[3] D. L. Perry, *Handbook of Inorganic Compounds*, 2nd ed. (CRC Press, Boca Raton, Florida, 2011).
[4] W. Lengauer, D. Rafaja, G. Zehetner, and P. Ettmayer, Acta Materialia **44**, 3331 (1996).
[5] F. T. J. Smith, Journal of Applied Physics **41**, 4227 (1970).
[6] A. Grill and P. R. Aron, Thin Solid Films **108**, 173 (1983).
[7] I. Suni, M. Mäenpää, M. A. Nicolet, and M. Luomajärvi, Journal of Electrochemical Society **130**, 1215 (1983).
[8] W. D. Sproul, Surface and Coatings Technology **36**, 191 (1988).
[9] M. Garbrecht, J. L. Schroeder, L. Hultman, J. Birch, B. Saha, and T. D. Sands, Journal of Materials Science **51**, 8250 (2016).
[10] L. García-González, L. Zamora-Peredo, N. Flores-Ramríez, M. G. Garnica-Romo, and J. Hernández-Torres, Journal of Materials Engineering and Performance **24**, 1558 (2015).
[11] H.-S. Seo, T.-Y. Lee, J. G. Wen, I. Petrov, J. E. Greene, and D. Gall, Journal of Applied Physics **96**, 878 (2004).
[12] S. Shinkai and K. Sasaki, Japanese Journal of Applied Physics **38**, 2097 (1999).
[13] M. Strømme, R. Karmhag, and C. G. Ribbing, Optical Materials **4**, 629 (1995).
[14] L. Yuan, G. Fang, C. Li, M. Wang, N. Liu, L. Ai, Y. Cheng, H. Gao, and X. Zhao, Applied Surface Science **253**, 8538 (2007).
[15] H.-S. Seo, T.-Y. Lee, I. Petrov, J. E. Greene, and D. Gall, Journal of Applied Physics **97**, 083521 (2005).
[16] M. Stoehr, H.-S. Seo, I. Petrov, and J. E. Greene, Journal of Applied Physics **99**, 043507 (2006).
[17] S. Chung, S. Shrestha, X. Wen, Y. Feng, N. Gupta, H. Xia, P. Yu, J. Tang, and G. Conibeer, Solar Energy Materials and Solar Cells **144**, 781 (2016).
[18] Y. Gotoh, S. Fujiwara, and H. Tsuji, Journal of Vacuum Science and Technology A **34**, 031401 (2016).
[19] Z. Gu, C. Hu, X. Fan, L. Xu, M. Wen, Q. Meng, L. Zhao, X. Zheng, and W. Zheng, Acta Materialia **81**, 315 (2014).
[20] R. Nowak and S. Maruno, Materials Science and Engineering A **202**, 226 (1995).
[21] K. Yamamoto, R. Noguchi, M. Mitsuhara, M. Nishida, T. Hara, D. Wang, and H. Nakashima, Journal of Applied Physics **118**, 115701 (2015).
[22] K. Yoshimoto, S. Shinkai, and K. Sasaki, Japanese Journal of Applied Physics **39**, 1835 (2000).
[23] T. Shimizu, M. Villamayor, D. Lundin, and U. Helmersson, Journal of Physics D: Applied Physics **49**, 065202 (2015).
[24] E.-J. Kim and D.-H. Kim, Electrochemical and Solid-State Letters **9**, C123 (2006).
[25] K. Matsumoto, Y. Itoh, and T. Kameda, Science and Technology of Advanced Materials **4**, 153 (2003).
[26] R. Nimmagadda and R. F. Bunshah, Thin Solid Films **63**, 327 (1979).

[27] R. A. Araujo, X. Zhang, and H. Wang, Journal of Electronic Materials **37**, 1828 (2008).
[28] I. L. Farrell, R. J. Reeves, A. R. H. Preston, B. M. Ludbrook, J. E. Downes, B. J. Ruck, and S. M. Durbin, Applied Physics Letters **96**, 071914 (2010).
[29] Y. Gotoh, H. Tsuji, and J. Ishikawa, in *Proceedings of the XII International Symposium on Sputtering and Plasma Processes (ISSP 2013)* (Kyoto, Japan, July 10–12, 2013), pp. 223–226.
[30] M. B. Takeyama, M. Sato, E. Aoyagi, and A. Noya, Japanese Journal of Applied Physics **53**, 02BC05 (2014).
[31] J. F. Kang, H. Y. Yu, C. Ren, M.-F. Li, D. S. H. Chan, X. Y. Liu, and D.-L. Kwong, Electrochemical and Solid-State Letters **8**, G311 (2005).
[32] H. Y. Yu, H. F. Lim, J. H. Chen, M. F. Li, C. Zhu, C. H. Tung, A. Y. Du, W. D. Wang, D. Z. Chi, and D.-L. Kwong, IEEE Electron Device Letters **24**, 230 (2003).
[33] H. Y. Yu, M.-F. Li, and D.-L. Kwong, IEEE Transactions on Electron Devices **51**, 609 (2004).
[34] T. Nozaki and Y. Hatano, International Journal of Hydrogen Energy **38**, 11983 (2013).
[35] W. D. Sproul, AIP Conference Proceedings **149**, 157 (1986).
[36] J. T. Gudmundsson, N. Brenning, D. Lundin, and U. Helmersson, Journal of Vacuum Science and Technology A **30**, 030801 (2012).
[37] U. Helmersson, M. Lattemann, J. Bohlmark, A. P. Ehiasarian, and J. T. Gudmundsson, Thin Solid Films **513**, 1 (2006).
[38] M. Lattemann, U. Helmersson, and J. E. Greene, Thin Solid Films **518**, 5978 (2010).
[39] F. Magnus, A. S. Ingason, O. B. Sveinsson, S. Olafsson, and J. T. Gudmundsson, Thin Solid Films **520**, 1621 (2011).
[40] H. Elmkhah, F. Attarzadeh, A. Fattah-Alhosseini, and K. H. Kim, Journal of Alloys and Compounds **735**, 422 (2018).
[41] F. Magnus, A. S. Ingason, S. Olafsson, and J. T. Gudmundsson, IEEE Electron Device Letters **33**, 1045 (2012).
[42] Y. P. Purandare, A. P. Ehiasarian, and P. E. Hovsepian, Journal of Vacuum Science and Technology A **29**, 011004 (2011).
[43] G. Berg, C. Friedrich, E. Broszeit, and K. H. Kloos, Surface and Coatings Technology **74-75**, 135 (1995).
[44] G. Abadias and P. Guerin, Applied Physics Letters **93**, 111908 (2008).
[45] R. Machunze and G. C. A. M. Janssen, Surface and Coatings Technology **203**, 550 (2008).
[46] R. Machunze, A. P. Ehiasarian, F. D. Tichelaar, and G. C. A. M. Janssen, Thin Solid Films **518**, 1561 (2009).
[47] U. B. Arnalds, J. S. Agustsson, A. S. Ingason, A. K. Eriksson, K. B. Gylfason, J. T. Gudmundsson, and S. Olafsson, Review of Scientific Instruments **78**, 103901 (2007).
[48] I. C. Noyan and J. B. Cohen, *Residual Stress: Measurement by Diffraction and Interpretation* (Springer-Verlag, New York, 1987).
[49] Q. Luo and A. H. Jones, Surface and Coatings Technology **205**, 1403 (2010).
[50] E. Török, A. J. Perry, L. Chollet, and W. D. Sproul, Thin Solid Films **153**, 37 (1987).
[51] S. Nagao, K. Nordlund, and R. Nowak, Physical Review B **73**, 144113 (2006).
[52] A. J. Perry, Thin Solid Films **193-194**, 463 (1990).
[53] B. O. Johansson, U. Helmersson, M. K. Hibbs, and J.-E. Sundgren, Journal of Applied Physics **58**, 3104 (1985).
[54] J. Bohlmark, M. Lattemann, J. T. Gudmundsson, A. P. Ehiasarian, Y. A. Gonzalvo, N. Brenning, and U. Helmersson, Thin Solid Films **515**, 1522 (2006).
[55] I. Blech and U. Cohen, Journal of Applied Physics **53**, 4202 (1982).
[56] R. Machunze and G. C. A. M. Janssen, Thin Solid Films **517**, 5888 (2009).
[57] F. Magnus, T. K. Tryggvason, S. Olafsson, and J. T. Gudmundsson, Journal of Vacuum Science and Technology A **30**, 050601 (2012).
[58] F. Magnus, O. B. Sveinsson, S. Olafsson, and J. T. Gudmundsson, Journal of Applied Physics **110**, 083306 (2011).
[59] J. T. Gudmundsson, Plasma Physics and Controlled Fusion **58**, 014002 (2016).
[60] J. T. Gudmundsson, D. Lundin, N. Brenning, M. A. Raadu, C. Huo, and T. M. Minea, Plasma Sources Science and Technology **25**, 065004 (2016).
[61] N. Brenning, J. T. Gudmundsson, M. A. Raadu, T. J. Petty, T. Minea, and D. Lundin, Plasma Sources Science and Technology **26**, 125003 (2017).
[62] C. Huo, M. A. Raadu, D. Lundin, J. T. Gudmundsson, A. Anders, and N. Brenning, Plasma Sources Science and Technology **21**, 045004 (2012).